Supplementary Information

Design of Bifunctional Janus Structure for High Efficiency Solar Distillation in Hypersaline Brine

Yun Han[1], Yunchen Du[1],*, Li Zhu[1], Yonglei Liu[1], Bo Hu[1], Bojing Sun[1],*, and Fei Han[1],*

[1]MIIT Key Laboratory of Critical Materials Technology for New Energy Conversion and Storage, School of Chemistry and Chemical Engineering, Harbin Institute of Technology, Harbin 150001, China

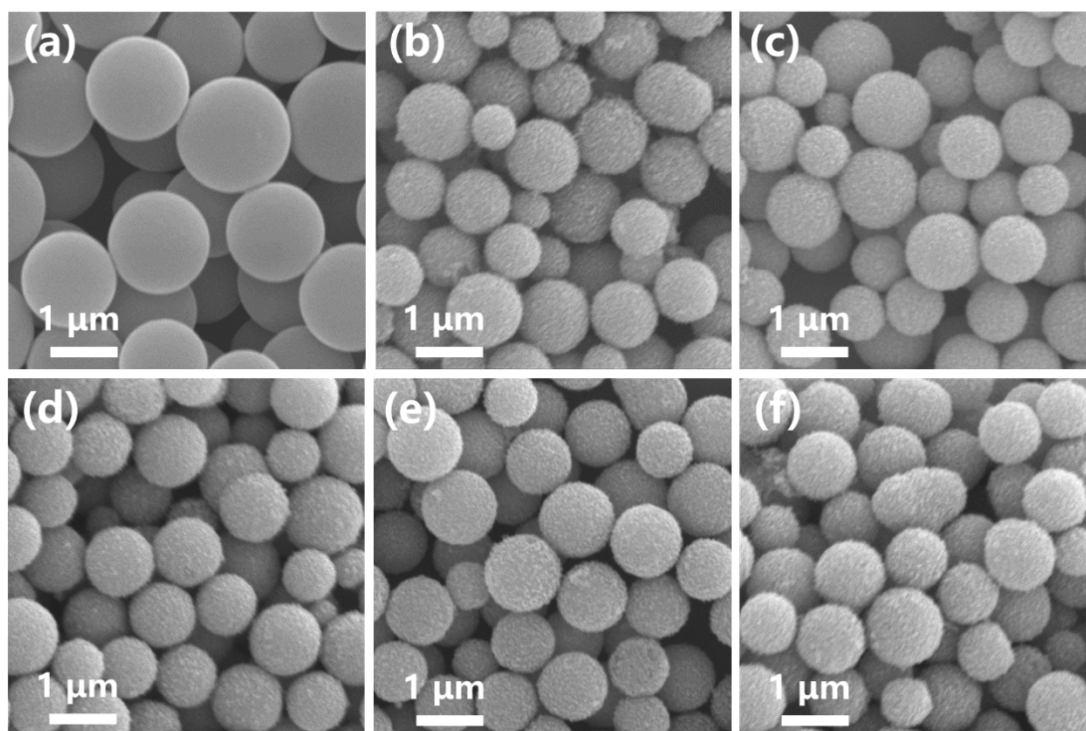E-mail: yunchendu@hit.edu.cn (Y. Du); sunbojing@ctgu.edu.cn (B. Sun); feihan@hit.edu.cn (F. Han).

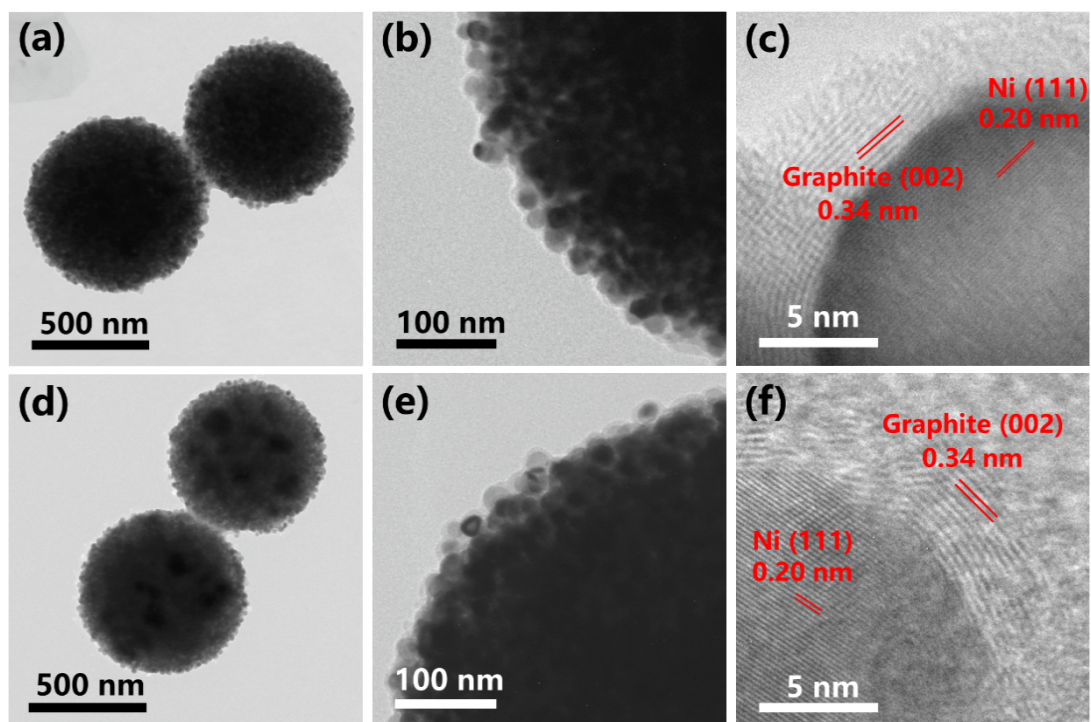**Fig. S1 a-f** SEM images of Ni-MOFs, Ni/C-*550*, Ni/C-*600*, Ni/C-*650*, Ni/C-*700*, and Ni/C-*750*.

Fig. S2 a, b TEM images of Ni/C-*700*. **c** HRTEM of Ni/C-*700*. **d, e** TEM images of Ni/C-*750*. **f** HRTEM of Ni/C-*750*.
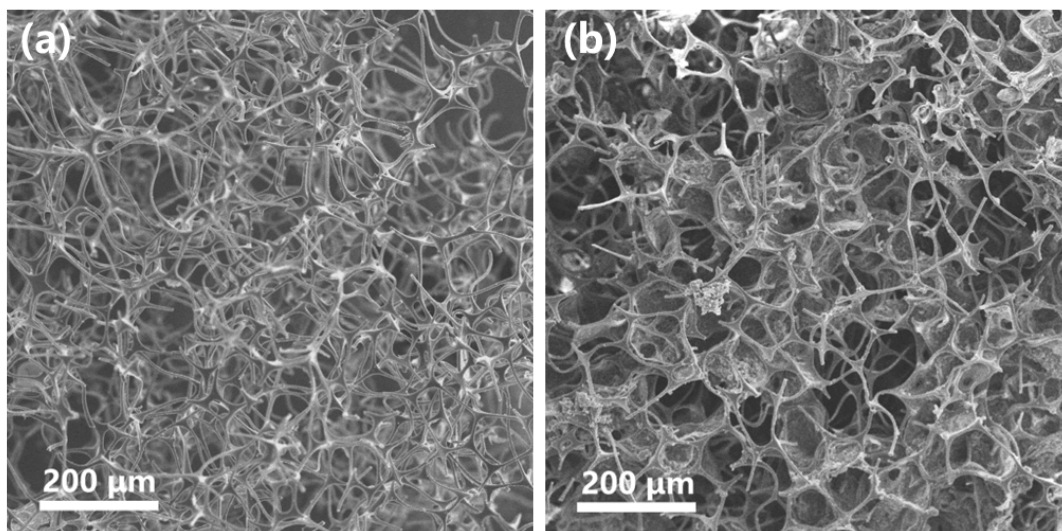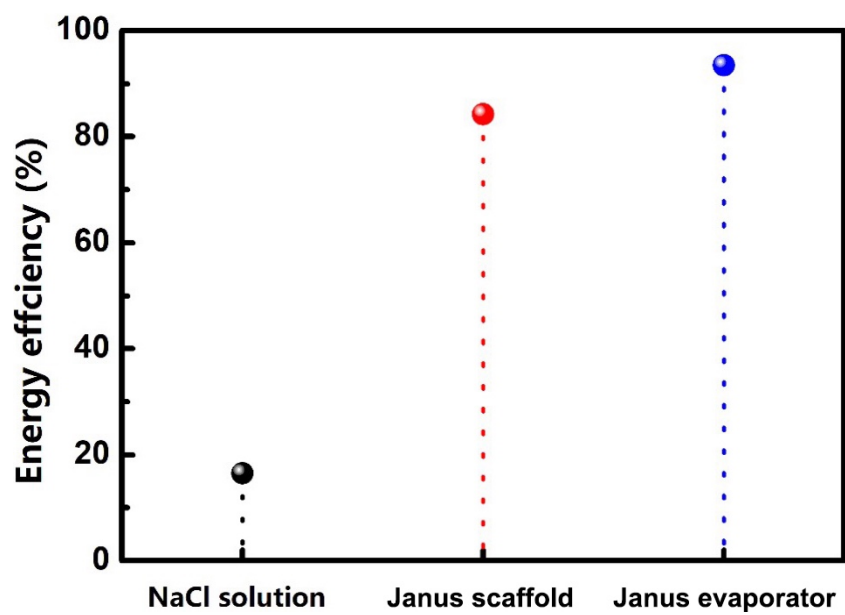
Fig. S3 a, b SEM images of MF, and MF with Ni/C.

Fig. S4 Energy efficiencies of 10.0 wt% NaCl solution evaporation without and with the aid of Janus scaffold and Janus evaporator.
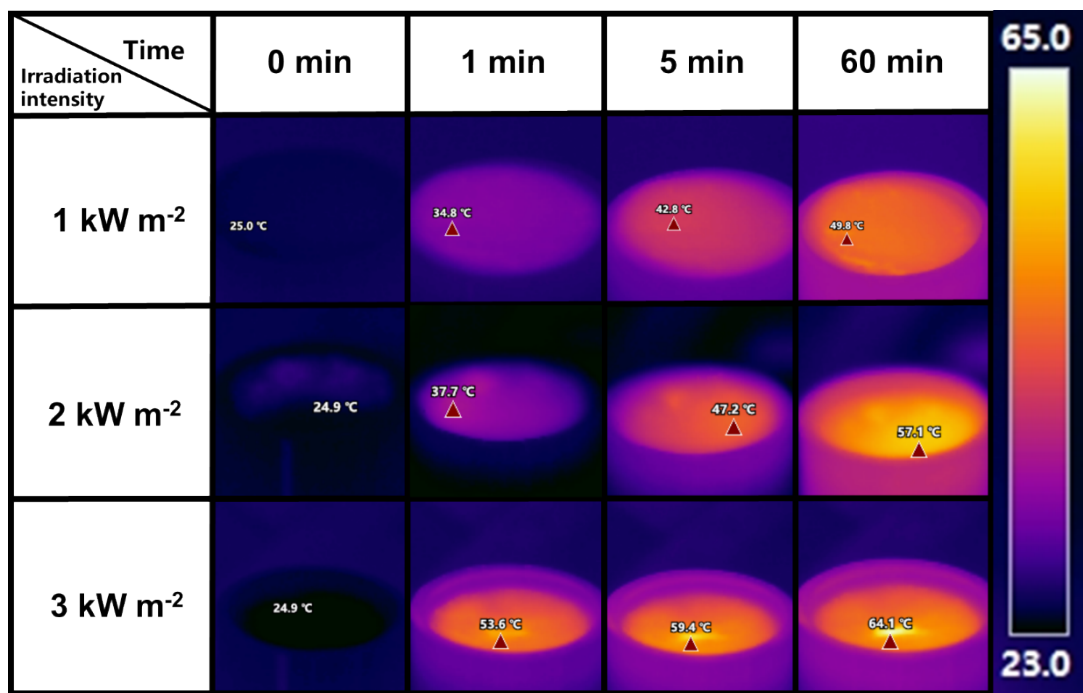
Time / Irradiation intensity	0 min	1 min	5 min	60 min
1 kW m^{-2}	25.0 ℃	34.8 ℃	42.8 ℃	49.8 ℃
2 kW m^{-2}	24.9 ℃	37.7 ℃	47.2 ℃	57.1 ℃
3 kW m^{-2}	24.9 ℃	53.6 ℃	59.4 ℃	64.1 ℃

Fig. S5 IR images of Janus evaporator over time under different irradiation intensities.
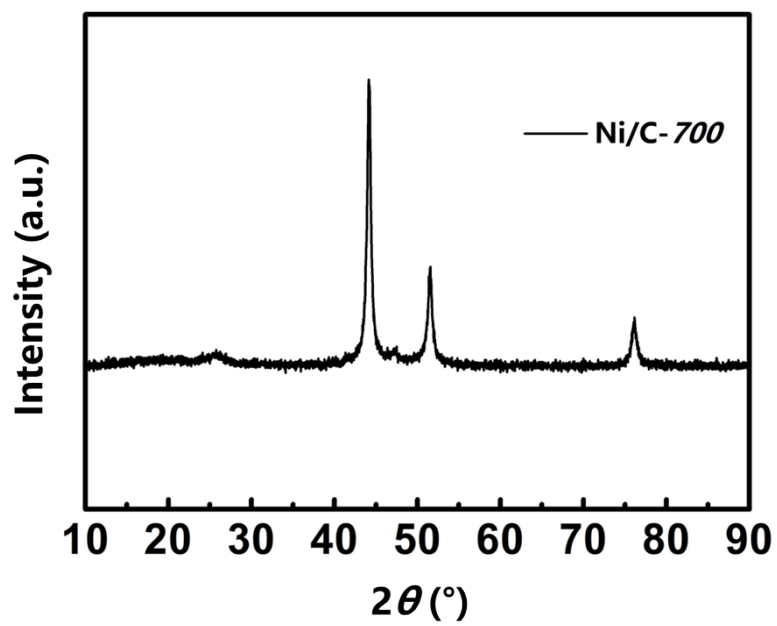
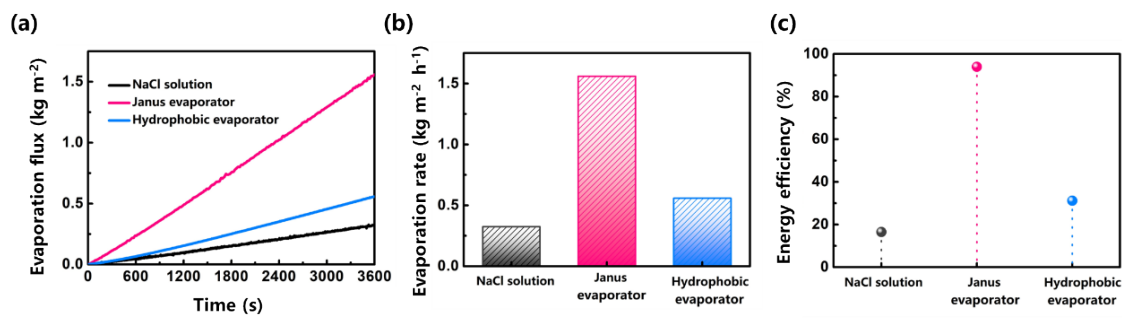**Fig. S6** XRD pattern of Ni/C-*700* after 12 hours irradiation in NaCl solution.

Fig. S7 a Evaporation flux variation. **b** Evaporation rates and **c** energy conversion efficiencies of 10.0 wt% NaCl solution with and without the aid of Janus evaporator and hydrophobic evaporator.
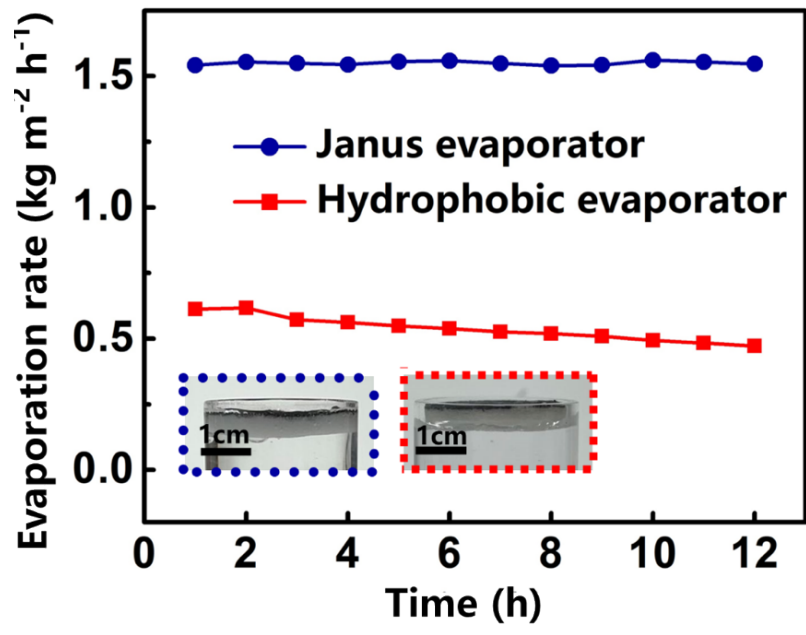
Fig. S8 Variation of the water evaporation rate of Janus evaporator and hydrophobic evaporator.
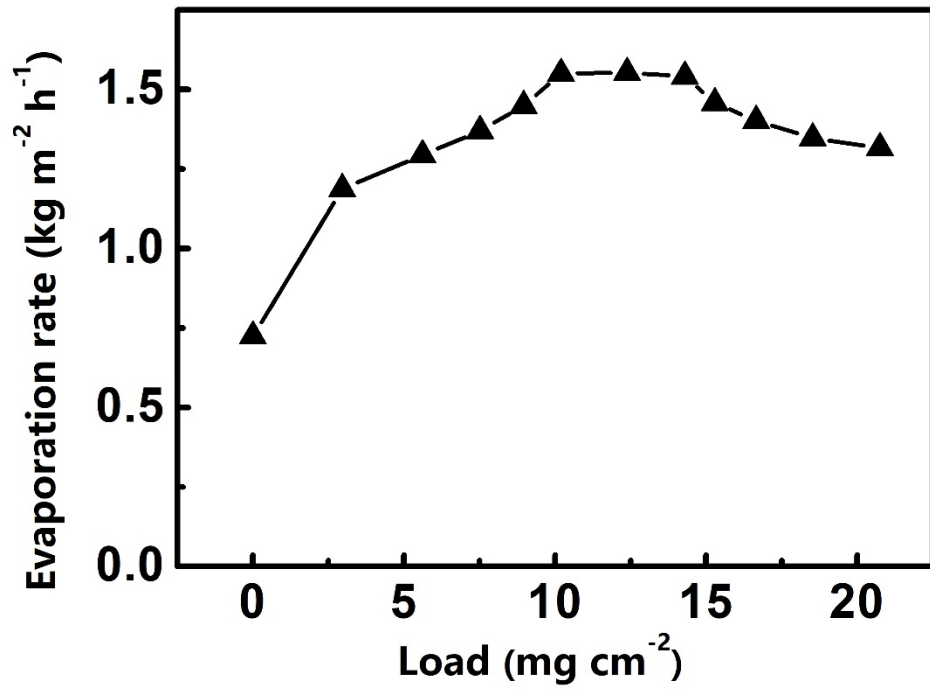
Fig. S9 Variation of the water evaporation rate with different Ni/C-*700* loading.
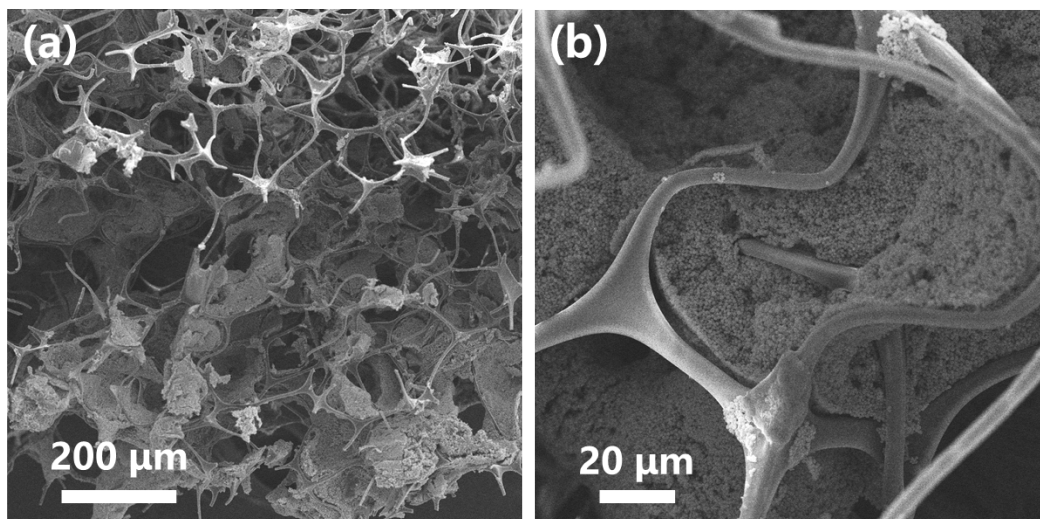
Fig. S10 SEM images with different resolutions of the upper layer of Janus evaporator at excessive loadings.
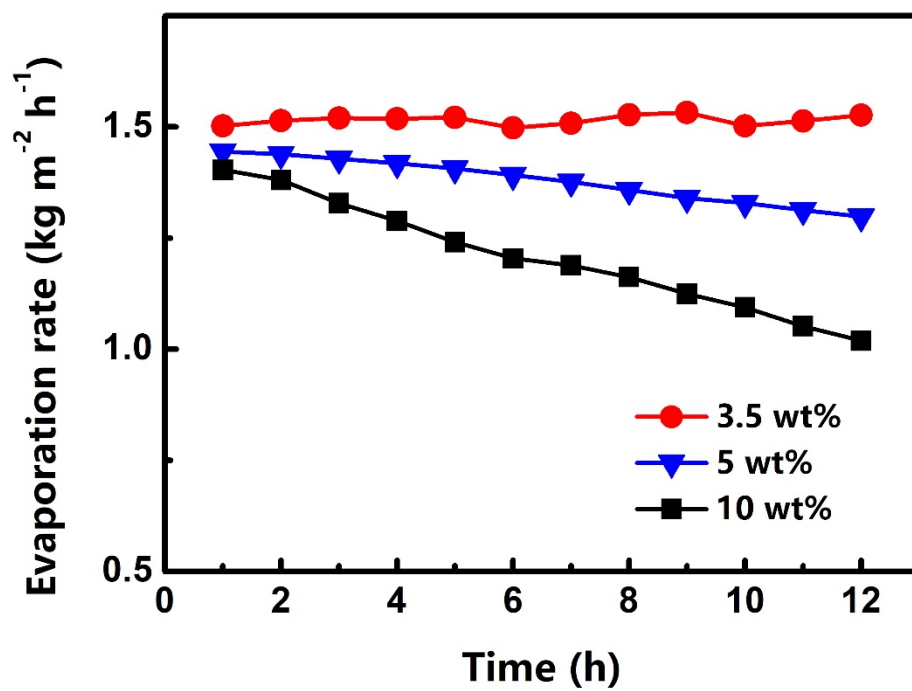
Fig. S11 Variation of evaporation rate with time for Janus scaffold operating in NaCl solutions with different concentrations.

Table S1 Water evaporation performance of evaporation ever published (under AM1.5 irradiation).

| Evaporator	Evaporation rate/ (kg m^{-2} h^{-1})	Salt concentration	Duration	reference
porous carbon polyhedron	2.74	seawater	10 h	[1]
Sandwich-Structured evaporator	2.67	seawater	27 h	[2]
MnO/C	2.15	seawater	30 h	[3]
CB/PMMA–PAN	1.3	3.5wt% NaCl	16 days	[4]
CB/ MF / EPE	1.24	3.5wt% NaCl	16 cycles	[5]
carbon fiber/ PEHG/ polystyrene foam	1.0	15 wt% NaCl	11 cycles	[6]
a water lily–inspired hierarchical structure	1.27	10 wt% brine	18 days	[7]
Our work	1.56	10 wt% NaCl	14 days	/
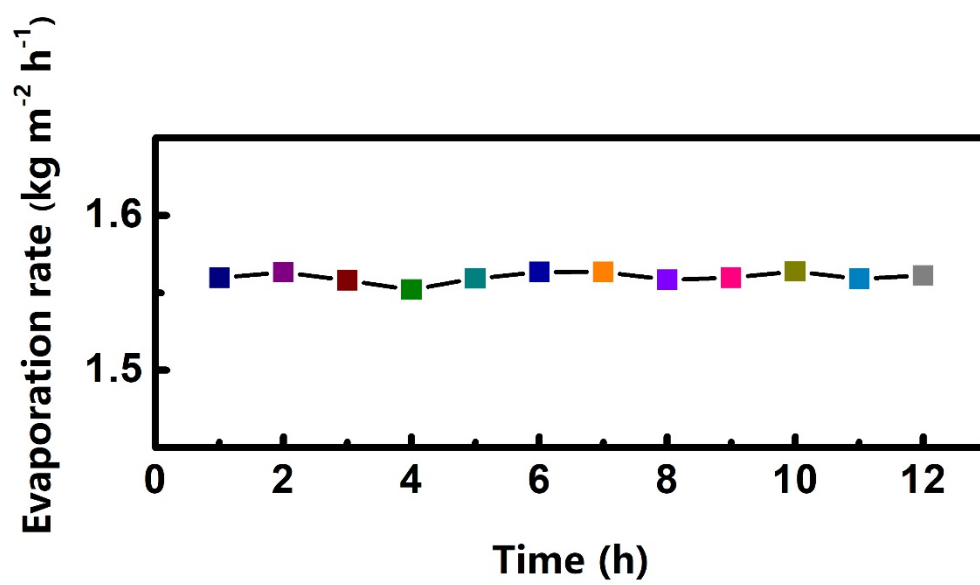
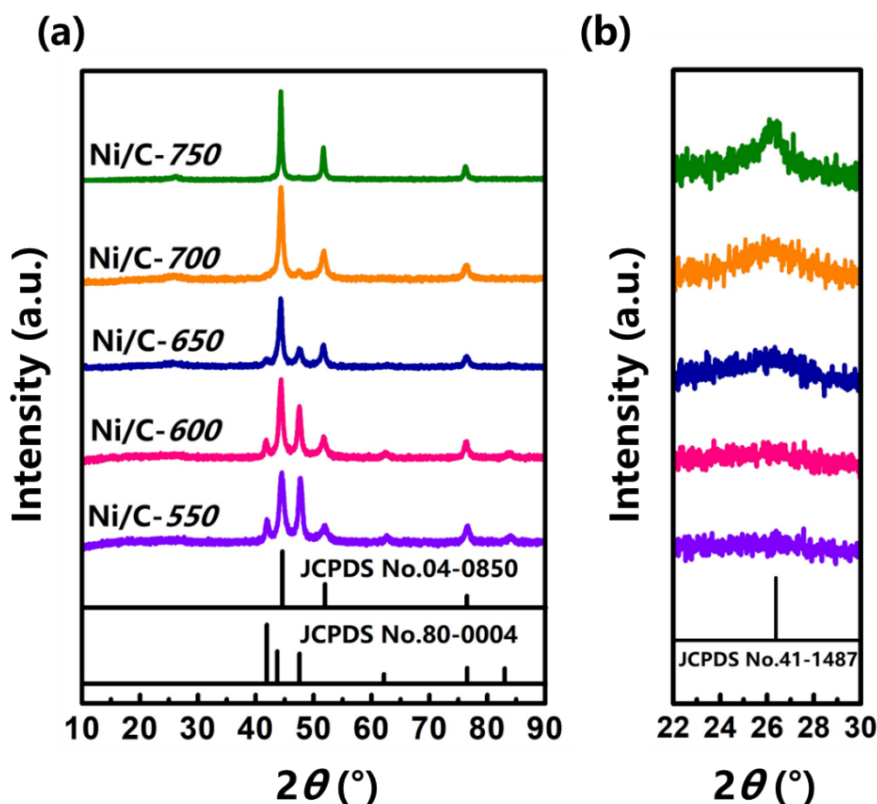**Fig. S12** Evaporation rate variation of Janus evaporator in Bohai seawater for 12h.

Fig. S13 a, b XRD patterns of Ni/C-*t* and the local enlargement in the 2θ range of 22°-30°.

The characteristic peaks at 44.51°, 51.81°, and 76.41° correspond to the (111), (200), and (220)

planes of face-centered cubic metal nickel (JCPDS No. 04-0850), respectively. With the

increase of pyrolysis temperature, the characteristic peaks of nickel gradually become sharp,

which may be because the high-temperature pyrolysis process improves the crystallinity of

nickel, and large particles of nickel appear at the same time [8]. The other characteristic peaks

in Ni/C-*550*, Ni/C-*600*, and Ni/C-*650* are precisely matched with crystalline carbon (JCPDS

No. 80-0004). A locally enlarged XRD pattern shows weak graphite (JCPDS No. 41-1487)

diffraction peaks at 26.3° in Ni/C-*650*, Ni/C-*700*, and Ni/C-*750*. Moreover, with the increase

in pyrolysis temperature, the diffraction peaks of crystalline carbon gradually weaken, and the

graphite diffraction peaks gradually sharpen, indicating that the crystalline carbon in the carbon

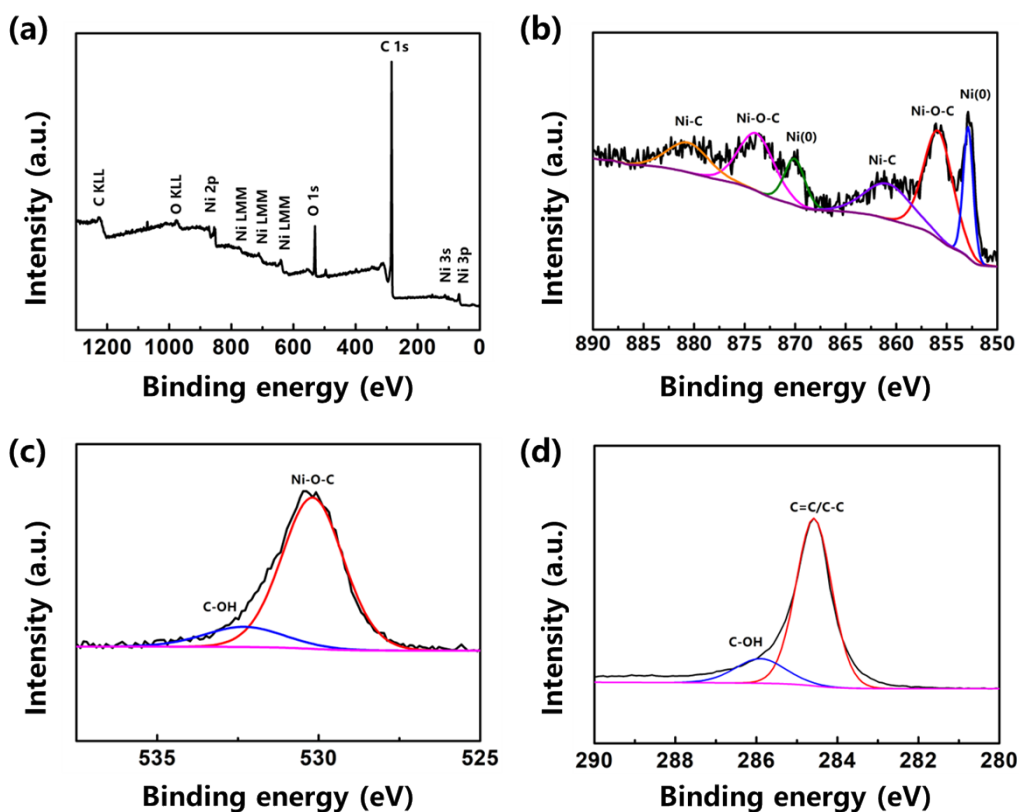shell can transform into graphitic carbon at high temperatures.

Fig. S14 XPS spectra of Ni/C-*700*: **a** survey scan spectrum; high resolution spectra of **b-d** Ni 2p, O 1s, and C1s, respectively.

As shown in the above figures, C, O, and Ni elements are detected, where the O may come from oxygen-containing functional groups in MOF synthesis. We note that the limited Ni ratio is because the nickel particles are encapsulated within the carbon shell, which cannot be readily detected. The peaks at 852.7 eV (Ni2p3/2) and 870.4 eV (Ni2p$_{1/2}$) are typical features of Ni(0) (Fig. S14b), and the Ni-C peaks appear at 860.9 eV (Ni2p$_{3/2}$) and 880.0 eV (Ni2p$_{1/2}$) [9,10]. The peaks stay at 855.8 and 874.1 eV may be attributed to Ni–O–C bond at the surface of Ni nanoparticles [10,11]. The O 1s spectrum can be deconvoluted into two peaks (Fig. S14c), which are assigned to C–O–Ni (530.2 eV) around the nickel core and surface C–OH (532.1 eV), respectively [11,12]. The two peaks in high resolution C 1s spectrum with binding energies of 284.6 and 285.9 indicate the presence of C=C/C-C and C-OH in the carbon shell

[11,13].
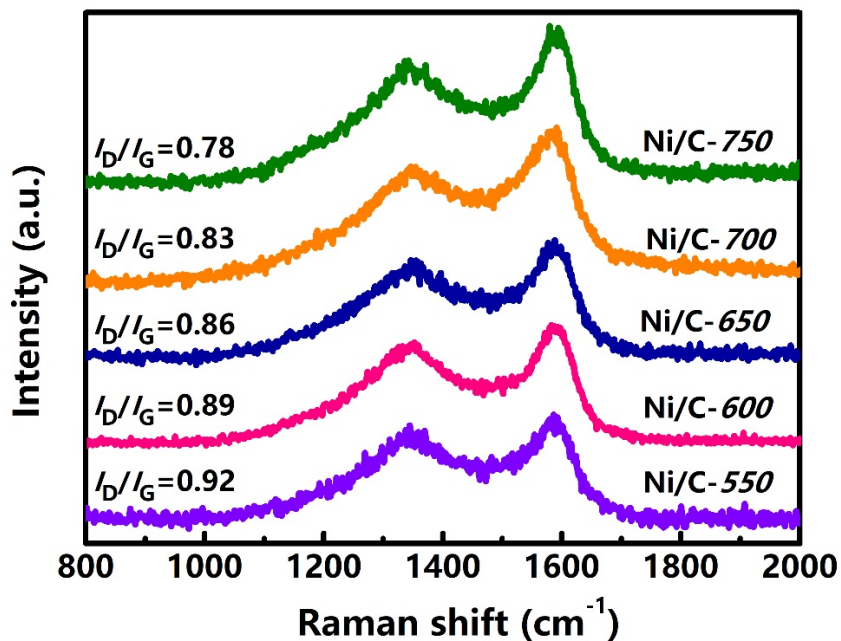
Fig. S15 Raman spectra of Ni/C-*t*.

There are two peaks in the range of 800-2000 cm^{-1}, the one at ~1350 cm^{-1} is defined as D band, and the other at ~1580 cm^{-1} is defined as G band. The intensity ratio of D and G band (I_D/I_G) is used to evaluate the relative graphitization of carbon materials [14,15]. The I_D/I_G values of Ni/C-*550*, Ni/C-*600*, Ni/C-*650*, Ni/C-*700*, and Ni/C-*750* are 0.92, 0.89, 0.86, 0.83, and 0.78, respectively. The values gradually decrease, which further indicates that the degree of graphitization gradually increases from Ni/C-*550* to Ni/C-*750*.

Fig. S16 TG curves of different Ni/C-*t*.

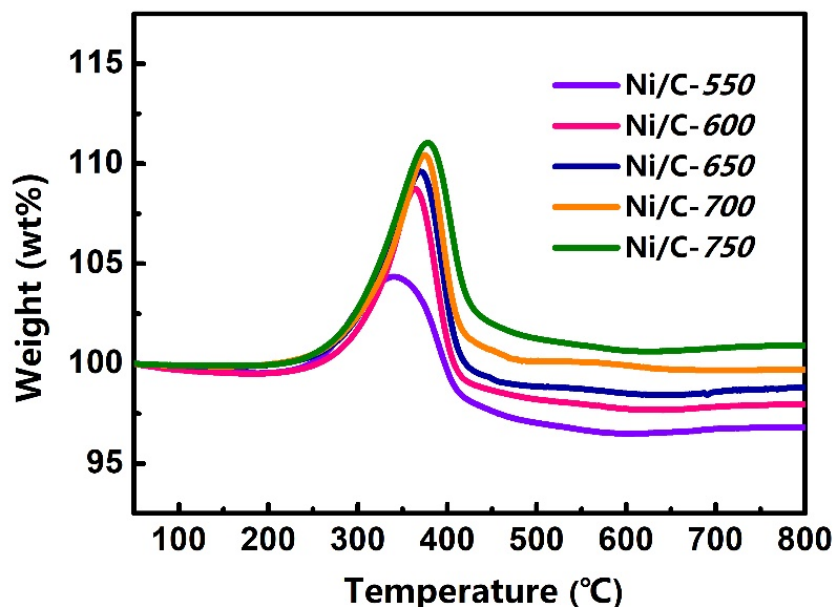To determine the carbon content in Ni/C, TG analysis was performed in air, from room temperature to 800°C with a temperature increase rate of 10°C/min. The weight increase in 200-370°C is caused by the oxidation of Ni. Another significant weight decreases at 370-550°C is caused by carbon combustion. As the temperature increases, the carbon is completely removed and the remaining mass (wt% R) after TG analysis is the mass of NiO. Thus, we deduce the carbon content in each sample based on the final mass and equation (2):

$$\frac{M(Ni)}{M(NiO)} wt\% R = 1 - wt\%_{carbon} \qquad (2)$$

where wt R%, wt % carbon, M(Ni), and M (NiO) refer to the remaining weight, carbon content, and formula amounts of Ni and NiO, respectively. The calculation results suggest that the specific contents of carbon in Ni/C-*550*, Ni/C-*600*, Ni/C-*650*, Ni/C-*700*, and Ni/C-*750* are 24.0 wt%, 23.0 wt%, 22.4 wt%, 21.6 wt%, and 20.7 wt%.
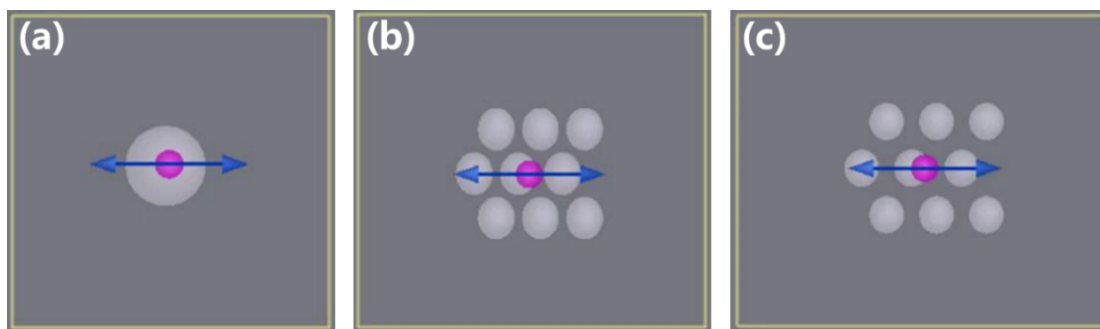
Fig. S17 Models for FDTD simulations. **a** A single Ni nanoparticle with a diameter of 500 nm. **b** A group of Ni nanoparticles with an average diameter of 20 nm and a spacing of 4 nm. **c** A group of Ni nanoparticles with an average diameter of 90 nm and a spacing of 40 nm.

References

1. H. J. Liu, L. J. Liu, Z. F. Fan, J. Liu, H. Y. Wang, et al., Transforming waste polyester into porous carbon polyhedron for interfacial solar steam and hydrovoltaic electricity co-generation. Chem. Eng. J. **485**, 149690 (2024). https://doi.org/10.1016/j.cej.2024.149690

2. R. Niu, J. Ren, J. J. Koh, L. Chen, J. Gong, et al., Bio-Inspired Sandwich-Structured All-Day-Round Solar Evaporator for Synergistic Clean Water and Electricity Generation. Advanced Energy Mater. **13**, 2302451 (2023). https://doi.org/10.1002/aenm.202302451

3. Z. Fan, J. Ren, H. Bai, P. He, L. Hao, et al., Shape-controlled fabrication of MnO/C hybrid nanoparticle from waste polyester for solar evaporation and thermoelectricity generation. Chem. Eng. J. **451**, 138534 (2023). https://doi.org/10.1016/j.cej.2022.138534

4. W. Xu, X. Hu, S. Zhuang, Y. Wang, X. Li, et al., Flexible and Salt Resistant Janus Absorbers by Electrospinning for Stable and Efficient Solar Desalination. Advanced Energy Mater. **8**, 1702884 (2018). https://doi.org/10.1002/aenm.201702884

5. G. Ni, S. H. Zandavi, S. M. Javid, S. V. Boriskina, T. A. Cooper, et al., A salt-rejecting floating solar still for low-cost desalination. Energy Environ. Sci. **11**, 1510-1519 (2018). https://doi.org/10.1039/c8ee00220g

6. Wei Zhao, Han Gong, Yan Song, Bo Li, Ning Xu, et al., Xu-Xiang ZhangJia Zhu, Hierarchically Designed Salt-Resistant Solar Evaporator Based on Donnan Effect for Stable and High-Performance Brine Treatment. Adv. Funct. Mater. **31**, 2100025 (2021). https://doi.org/10.1002/adfm.202100025

7. W. Zhao, H. Gong, Y. Song, B. Li, N. Xu, et al., A water lily-inspired hierarchical design for stable and efficient solar evaporation of high-salinity brine. Sci Adv. **5**, eaaw7013 (2019). https://doi.org/10.1126/sciadv.aaw7013

8. B.D. Hall, D. Ugarte, D. Reinhard, R. Monot, Calculations of the dynamic debye–scherrer diffraction patterns for small metal particles. J. Chem. Phys. **103**, 2384-2394 (1995). https://doi.org/10.1063/1.469662

9. L. L. Fan, P. F. Liu, X. C. Yan, L. Gu, Z. Z. Yang, H. G. Yang, S. L. QiuX. D. Yao, Atomically isolated nickel species anchored on graphitized carbon for efficient hydrogen evolution electrocatalysis. Nat. Commun. **7**, 10667 (2016). https://doi.org/10.1038/ncomms10667

10. P. Shanmugam, A. P. Murthy, J. Theerthagiri, W. Wei, J. Madhavan, H.-S. Kim, T. MaiyalaganJ. Xie, Robust bifunctional catalytic activities of N-doped carbon aerogel-nickel composites for electrocatalytic hydrogen evolution and hydrogenation of nitrocompounds. International Journal of Hydrogen Energy **44**, 13334-13344 (2019). https://doi.org/10.1016/j.ijhydene.2019.03.225

11. X. Guo, H. Kan, X. Liu, H. GengL. Wang, Facile synthesis of hollow hierarchical Ni@C nanocomposites with well-dispersed high-loading Ni nanoparticles embedded in carbon for reduction of 4-nitrophenol. RSC Adv. **8**, 15999-16003 (2018). https://doi.org/10.1039/c8ra02281j

12. Y. Yang, J. Liu, S. Guo, Y. LiuZ. Kang, A nickel nanoparticle/carbon quantum dot hybrid

as an efficient electrocatalyst for hydrogen evolution under alkaline conditions. J. Mater. Chem. A **3**, 18598-18604 (2015). https://doi.org/10.1039/c5ta04867b

13. Y. Qiu, Y. Lin, H. Yang, L. Wang, M. WangB. Wen, Hollow Ni/C microspheres derived from Ni-metal organic framework for electromagnetic wave absorption. Chem. Eng. J. **383**, 13207 (2020). https://doi.org/10.1016/j.cej.2019.123207

14. A.C. Ferrari, J. Robertson, Interpretation of raman spectra of disordered and amorphous carbon. Phys. Rev. B **61**, 14095-14107 (2000). https://doi.org/10.1103/PhysRevB.61.14095

15. L.A. Lyon, C.D. Keating, A.P. Fox, B.E. Baker, L. He, et al., Raman spectroscopy, Anal.Chem. **70**, 341R-361R (1998). https://doi.org/10.1021/a1980021p